UNIVERSITY OF CALIFORNIA, IRVINE

Investigating Vesicle Behavior with Atomic Force Microscopy - Force Spectroscopy

THESIS

submitted in partial satisfaction of the requirements

for the degree of

MASTER OF SCIENCE

in Materials Science & Engineering

by

Evangeline Wong

Thesis Committee:

Associate Professor Regina Ragan, Chair

Associate Professor Daniel Mumm

Professor Szu-Wen Wang

2018

CONTENTS

LIST OF FIGURES

ABSTRACT

Investigating Vesicle Behavior with Atomic Force Microscopy - Force Spectroscopy

By

Evangeline Wong

Master of Science in Materials Science & Engineering, 2018

University of California, Irvine

Professor Regina Ragan, Chair

Investigating the mechanical behavior of lipid bilayer membranes is essential to understanding important cellular processes, such as morphogenesis, motility, drug delivery, mechanotransduction, metastasis, and focal adhesion. The mechanical properties of 1-palmitoyl-2-oleoyl-*sn*-glycero-3-phosphocholine (POPC) vesicles grafted with different 1,2-distearoyl-*sn*-glycero-3-phosphoethanolamine-*N*-poly(ethylene glycol)-2000-*N*-[3-(2-pyridyldithio) propionate] (DSPE-PEG-PDP) concentrations were studied using Atomic Force Microscopy-Force Spectroscopy (AFM-FS) under buffer environment. The concentration of DSPE-PEG-PDP incorporated into POPC vesicles was systematically varied from 0 mol% to 10 mol%. By increasing DSPE-PEG-PDP concentration from 0 – 10 mol%, vesicle size decreases, breakthrough distance increases, breakthrough force decreases, and the Young's modulus decreases slightly. We also observe two E values exist at 5%, suggesting the existence of two conformations. PEG-grafted vesicles are sterically stabilized due to the presence of dangling PEG chains outside the vesicle membrane. The aim of this study is to examine the relationship between vesicle rigidity and vesicle stability.

CHAPTER 1. INTRODUCTION

1.1 Motivation

Since the mechanical properties of mesoscopic structures such as bone, muscle, and tendons are important for their functions, then we can deduce that these properties are equally important on the nanometric scale and will determine the behavior of single proteins and their assemblies[1]. The mechanical properties of single cells are known to reflect their physiological state and to be altered in some pathological states such as cancer[1]. Understanding the mechanical behavior of vesicles to design specific properties for more effective vesicle applications, such as a vehicle for drug delivery or as a model of biological membranes, requires studies of model systems. The nanomechanical properties of the membrane envelope, such as stiffness, surface elastic response, and adhesion, impact cellular processes[2], such as morphogenesis[3,4], motility[5,6], drug delivery[7–10], mechanotransduction[11], metastasis[12], and focal adhesion[13], therefore studying the effect of mechanical stress on membranes is important for understanding cell dynamics.

This study examines vesicle rupture mechanics with atomic force microscopy - force spectroscopy to elucidate the mechanical behavior of vesicles by investigating the relationship between vesicle rigidity and vesicle stability as well as quantifying the Young's modulus. The model system used was 1-palmitoyl-2-oleoyl-*sn*-glycero-3-phosphocholine (POPC) vesicles grafted with 1,2-distearoyl-*sn*-glycero-3-phosphoethanolamine-*N*-poly(ethylene glycol)-2000-*N*-

[3-(2-pyridyldithio) propionate] (DSPE-PEG-PDP). We see these chemical structures in Figure 1.

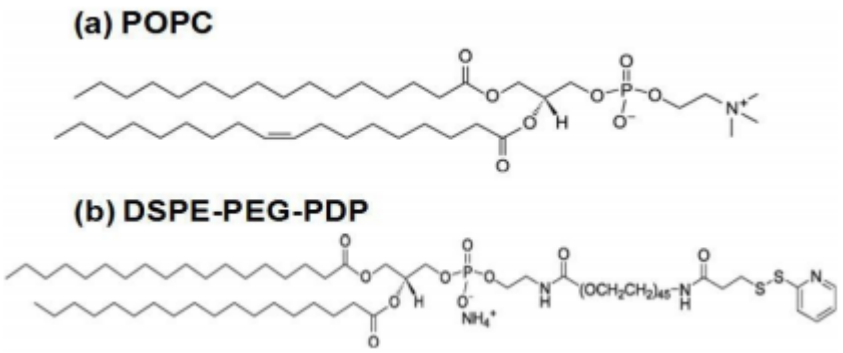

Figure 1. Chemical structure of lipids used in this study: (a) POPC is the primary component in tLBMs; (b) DSPE-PEG-PDP molecule with disulfide group is used for Au-thiolate bond formation[14].

DSPE-PEG-PDP concentrations were varied from 0 mol% to 10 mol%, and were studied using atomic force microscopy - force spectroscopy under a buffer environment. This particular system is used because POPC is commonly used to build model cell membranes, since 40-50% of the myriad phospholipid species in mammalian cell membranes are zwitterionic phophatidylcholine (PC), causing cell surfaces to primarily have a neutral charge[15,16]. DSPE-PEG-PDP was chosen due to a disulfide group that can form Au-thiolate bonds between gold and functionalized POPC vesicles, which increases vesicle-substrate interactions[17–20]. Atomic force microscopy - force spectroscopy (AFM-FS) is a characterization technique that enables us to examine the mechanical properties of samples in solution at the nanoscale level[21,22].

CHAPTER 2. BACKGROUND

2.1 Biophysical System

Lipid bilayers are a model system to understand biomembrane function, because since they compose the membrane enveloping cells and vesicles, they serve a structural role under a complex combination of cell-cell, cell-matrix, and flow forces[23], such as the high forces sensed by chondrocytes in the cartilage matrix to the relatively low flow forces sensed in kidney tubules[23–26]. They also contribute to the function of membrane proteins, such as mechanosensitive ion channels[27,28].

Alterations in the stiffness of lipid bilayers affect the modulation of membrane protein function[29]. One factor impacting lipid membrane stiffness is lipid saturation. Saturated lipids form stiffer membranes, because single-bonded backbone carbons can freely orient themselves into tightly-packed structures, while unsaturated lipids form more fluid membranes, because kinks resulting from double-bonded backbone carbons prevent them from freely orienting into optimally-packed structures. A vesicle's stiffness also increases when an abundance of lipids are embedded in a vesicle membrane, and crowding in the interior of the vesicle occurs. Nanomechanical properties of the membrane envelope, such as stiffness, surface elasticity, and adhesion, play an important role in cellular processes, such as morphogenesis[3,4], motility[5,6], drug delivery[7–10], mechanotransduction[11], metastasis[12], and focal adhesion[13], which encourages an examination of the mechanical properties of vesicles.

2.2 Characterization

Atomic Force Microscopy (AFM)[30] has become an invaluable tool for studying the structure and mechanical properties of molecular systems, because of its ease of use, sensitivity and versatility as a stand-alone, high-resolution imaging technique and force transducer. The main strength of AFM for this work is its capability to operate in an aqueous environment on a wide variety of biological samples, from single molecules – DNA or proteins – to macromolecular assemblies like biological membranes[31]. The main advantage with respect to other techniques is that the structure of biological samples, such as cell or lipid membranes can be visualized, not only in liquid media, but in real time with nanometer resolution[32,33], such as when studying native plasma membranes isolated from eye lens[34].

AFM force spectroscopy (FS) can be used to sense and apply forces with pN sensitivity. It is an excellent tool to gather information about molecular interactions at the single molecule level[35–38]. AFM-FS studies are valuable to study properties of lipid bilayers and contribute to the comprehension of fundamental aspects concerning the structural, mechanical, and biological properties of membranes. Applying AFM-FS to membrane proteins increases our knowledge about the intra- and inter-molecular interactions of these proteins with the cell membrane, which are relevant to drive protein folding, oligomerization and functional activity[39]. With the ability to measure surface forces at the nanoscale, AFM-FS is a valuable technique for studying the van der Waals interactions and adhesion forces prevalent in biophysical systems, such as blood cells[40], neurons[41,42], tumors[43,44], and the interaction of graphene oxide with bacterial cell membranes[45], providing a new perspective on membrane mechanics in confined areas within the nanometer realm, where most specific molecular interactions take place.

2.3 Mechanical Models

The mechanical properties of 1-palmitoyl-2-oleoyl-*sn*-glycero-3-phosphocholine (POPC) vesicles grafted with different 1,2-distearoyl-*sn*-glycero-3-phosphoethanolamine-*N*-poly(ethylene glycol)-2000-*N*-[3-(2-pyridyldithio) propionate] (DSPE-PEG-PDP) concentrations were studied using AFM force spectroscopy under buffer environment. The concentration of DSPE-PEG-PDP incorporated into POPC vesicles was systematically varied from 0 mol% to 10 mol%. In order to understand the AFM data generated from AFM-FS, we need mechanical models that clarify the interaction between the AFM-FS probe tip and substrate. Mechanical models, such as the Hertz Model, the Sneddon Model, and the Bottom Edge Cone Correction Model, elucidate the interaction behavior between an AFM-FS probe and a sample of interest. Since we are studying vesicle rupture mechanics and the mechanical properties of vesicles, comparing these three mechanical models enables us to understand how structure and chemical environment affect stability. This is important when designing the triggered release of internal payloads from vesicular structures for drug delivery applications[46].

2.3.1 Hertz Model

The classical model of contact mechanics, the *Hertz model*, approximates the AFM-FS probe tip as a sphere that indents an infinite thick film when the radius of the spherical tip is much greater than the indentation[47–49]. Therefore it works well when using microbeads at the end of the AFM tip[50–52], though this yields low resolution. It has been used to study the elastic properties of soft materials such as prostate cancer cells[53], living fibroblasts[54], and hydrogels[55]. The Hertz model is commonly used to determine the zero-frequency Young's modulus from AFM data[56] by

calculating contact stress between the probe tip and sample surface as the stress around the contact area between two spheres of different radii. Load (F) versus indentation depth (δ) is related by[48]:

$$F = \frac{4}{3}\frac{ER^{1/2}\delta^{3/2}}{(1-v^2)}$$

where E is the Young's modulus of the materials. ν is the Poisson's ratio of 0.5 for vesicles considered as incompressible materials in response to uniaxial strain[16,57,58]. The Hertz model works well when using microbeads at the end of the AFM tip[50–52], but this yields low resolution.

2.3.2 Sneddon Model

In place of the simplification of the AFM-FS probe tip as a sphere in the Hertzian model, the Sneddon model considers the probe tip as a conical or paraboloidal tip indenting on a semi-infinite thick film[16], taking into consideration the opening angle of a conical tip, therefore this model is more applicable to higher resolution tips. It is commonly used to model the elastic properties of soft materials such as endothelial cells[59], adsorbed hydrophobically modified inulin films on latex particles[60], and HeLa cells[61]. Load (F) versus indentation depth (δ) is related by[62]:

$$F_{cone} = \frac{2}{\pi}\tan\alpha\ \frac{E}{1-v^2}\delta^2$$

where α is the opening angle of a conical tip (35 degrees); E is the Young's modulus of the film; and v is the Poisson's ration of tLBMs equal to 0.5 assuming a perfectly incompressible material in response to uniaxial strain[16,57,58]. The Sneddon model is a better fit for higher resolution tips

than the Hertz model, but finite thickness differences of the film and substrate cause force spectroscopy data to yield overestimate the value of E.

2.3.3 Bottom Effect Cone Correction

Bottom Effect Cone Correction (BECC) improves the Sneddon model by using the Betti-Rayleigh reciprocal theorem to correct for finite thickness differences of the film and substrate that cause analysis of force spectroscopy data to generate calculated E values higher than the actual E value when using the Sneddon model. BECC has been applied to studies of actomyosin stress fibers[63], cancer cells[44], and the erythrocyte membrane[40]. Load (F) versus indentation depth (δ) is related by[64]:

$$F_{BECC} = \frac{8}{3\pi} E \tan\theta \delta^2 \left(1 + 1.7795 \frac{2\tan\theta}{\pi^2} \frac{\delta}{h} + 16(1.7795)^2 \tan^2\theta \frac{\delta^2}{h^2} \right)$$

where α is the opening angle of a conical tip (35 degrees); E is the Young's modulus of the film; and v is the Poisson's ration of tLBMs equal to 0.5 assuming a perfectly incompressible material in response to uniaxial strain[16,57,58]. BECC is better than the Sneddon model, because it corrects for the Sneddon model's overestimation of E.

2.3.4 Summary

The Hertz model works well for spherical AFM tips, such as microbeads, but it yields low resolution. The Sneddon model, on the other hand, treats tips as cones or parabaloids, therefore it is a better model than the Hertz model for higher resolution tips. However, the BECC model improves the Sneddon model by accounting for finite thickness differences of the film and

substrate that yield calculated E values that are higher than the expected actual value. Thus, the BECC model generates better results than the previously-mentioned models.

CHAPTER 3. METHODS

3.1 Vesicle Fabrication

3.1.1 Materials

1-Palmitoyl-2-oleoyl-*sn*-glycero-3-phosphocholine (POPC) and 1,2-distearoyl-*sn*-glycero-3-phosphoethanolamine-*N*-poly(ethylene glycol)-2000-*N*-[3-(2-pyridyldithio) propionate] (DSPE-PEG-PDP) were obtained from Avanti Polar Lipids (Alabaster, AL). HEPES at >99.5% purity and chloroform at >99.8% purity were purchased from Sigma-Aldrich (St. Louis, MO). NaCl at >99.0% purity was from Fisher Scientific Inc. (Pittsburgh, P A). Water used in this study was purified with a Milli-Q water system (≥ 18.2 MΩ.cm, Millipore Corp., Billerica, MA). All chemicals were used as received.

3.1.2 Preparation of Unilamellar Vesicles

Large unilamellar vesicles were prepared following an extrusion method[17,65]. Vesicles were prepared with lipids composition of (i) 0 mol% DSPE-PEG-PDP/100 mol% POPC, (ii) 2.5 mol% DSPE-PEG-PDP/97.5 mol% POPC, (iii) 5 mol% DSPE-PEG-PDP/95 mol% POPC, and (iv) 10 mol% DSPE-PEG-PDP/90 mol% POPC. DSPE-PEG-PDP and POPC lipids were dissolved in chloroform at 1 mg/mL for stock solutions. Lipids were mixed at desired molar ratios upon using. The lipids in chloroform mixture were dried on the bottom of a glass vial by a gentle stream of nitrogen and desiccated in vacuum for at least 1 h to completely remove chloroform. Then, the dried lipid mixtures were rehydrated by the addition of HEPES buffer (5 mM HEPES, pH 7.4, with 150 mM NaCl) to yield a final lipid concentration of 5 mM. The resulting lipid suspensions were then subjected to five freeze-thaw cycles and extruded 15 times through two polycarbonate

membranes with a pore size of 100 nm using a syringe-type extruder (Avanti Polar Lipids, Alabster, AL).

3.1.3 Sample Preparation

A 100 μL aliquot of vesicle suspension with lipid concentration of (i) 0% DSPE-PEG-PDP/100% POPC, (ii) 2.5% DSPE-PEG-PDP/97.5% POPC, (iii) 5% DSPE-PEG-PDP/95% POPC, (iv) 10% DSPE-PEG-PDP/90% POPC were deposited on an 8 mm × 8 mm Au substrate glued in a fluid cell. Au substrates were prepared via template stripping (TS) method to create a pristine and atomically flat surface[66]. Vesicles were stabilized on a TS Au substrate at room temperature for 5 min. Additional 2 mL HEPES buffer was then added to the fluid cell to keep the sample hydrated and maintain a low vesicle concentration during AFM characterization.

3.2 AFM Force Spectroscopy

AFM allows the local probing of the mechanical properties of a lipid bilayer by exploiting the force spectroscopy technique[67–71]. During a force spectroscopy measurement, the AFM tip briefly presses on the supported lipid bilayer and after an initial elastic interaction related to indentation of the lipid bilayer, at a critical force value, the tip jumps through the bilayer and goes immediately in contact with the underlying support, the substrate. The force value corresponding to the breakthrough, or jump through, event marks the bilayer's stability and the strength of the fluctuations in the bilayer[72]. Several reviews can be found in the literature dealing with the force spectroscopy technique for the study of supported lipid bilayers[71,73,74].

AFM force spectroscopy was performed using a MFP-3D-Bio AFM (Asylum Research, Santa Barbara, CA). Commercial silicon nitride AFM probes (OMCL-TR 400 PSA, Olympus) with pyramid-shaped tips and Au coating on the reflective side of a cantilever with a nominal spring constant of 0.08 N/m were used for AFM measurements. The radius of curvature of the AFM tip is 20 ± 5 nm, as provided by the manufacturer. AFM force spectroscopy was carried out at room temperature in HEPES buffer under contact mode. Before force measurement, the AFM cantilever spring constant was calibrated by measuring deflection against a hard reference substrate and then by the thermal noise method[75].

To acquire force curves from vesicles, force mapping in a 32 × 32 array grid pattern was performed at randomly approached sample positions. Before force mapping, sample topography was not imaged with AFM to prevent rupture of adsorbed vesicles[76]. Force measurements were performed with an approaching speed of 1.8 μm/s. In each force measurement cycle, AFM tip retraction was initiated at a trigger force of 3 nN. Only force curves with two breakthrough events attributed to AFM tip penetration through vesicles were analyzed.

3.3 Computational Data Processing

3.3.1 Approach point and physics of tip-surface interactions

When an AFM tip is brought close to a sample, the forces typically contributing the most to the movement of an AFM cantilever are *coulombic* and *van der Waals* interactions. Figure 2 is a plot of force against distance illustrating the relationship between repulsive forces (coulombic interactions), attractive forces (van der Waals interactions), and the force response curve (force-distance curve).

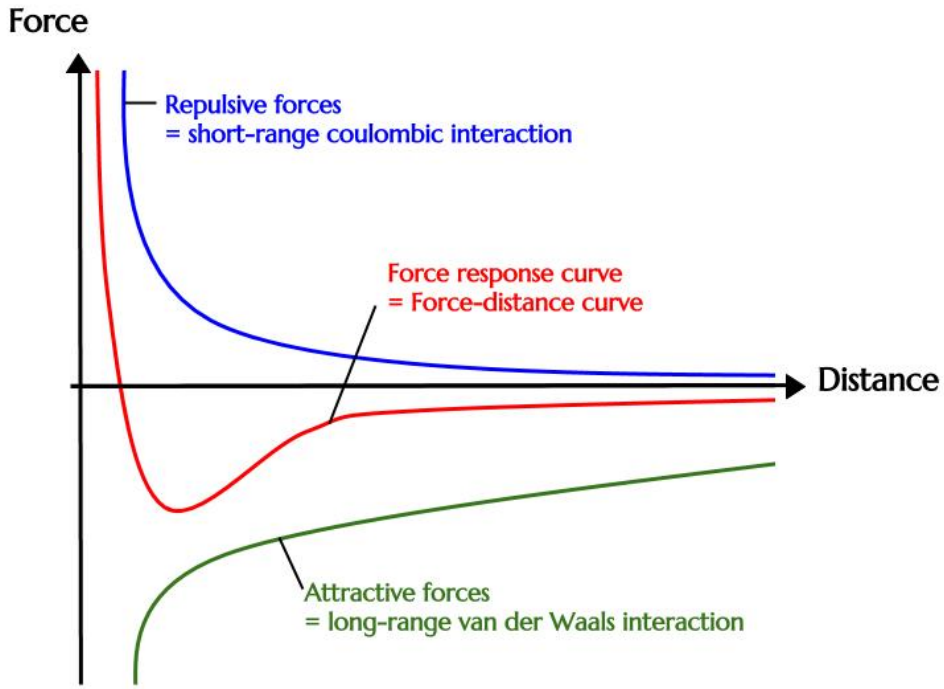

Figure 2. Plot of force against distance illustrating the relationship between repulsive forces (coulombic interactions, blue curve), attractive forces (van der Waals interactions, green curve), and the force response curve (force-distance curve, green curve).

Coulombic interactions are the strong, short-range repulsive force arising from electron repulsion by electron clouds surrounding the tip and sample. This repulsion increases as the separation decreases. *Van der Waals* interactions are longer-range attractive forces arising due to temporary fluctuating dipoles. As the tip nears a sample, van der Waals forces cause attraction, which increases as the tip gets closer to the sample. At small separations the repulsive coulombic forces dominate and cause the cantilever to bend as the tip approaches the surface. The combination of coulombic interaction and van der Waals interaction results in a force-distance curve similar to the red curve in Figure 2, Figure 3c and Figure 4.

Figure 3a is a tapping-mode AFM topography image of mica after exposure to POPC vesicles. The yellow domain is a POPC lipid bilayer membrane (LBM) patch. The height of LBM measured from the corresponding line profile is 4.2 nm as shown in Figure 3b. AFM force measurements can be used to confirm the presence of LBM on the substrate, especially when LBM forms a continuous layer on the substrate and a topography image could not determine the existence of LBM[14]. Figure 3c is a representative force-distance curve obtained on the yellow LBM region shown in Figure 3a. The schematic in Figure 3d describes tip-sample interaction in a force measurement cycle. AFM probe approaches the membrane without tip-sample interaction from point 'A' until initial interaction with the membrane surface at point 'B'. Between point 'B' and 'C', an AFM probe compresses the soft membrane. Until the force applied by the AFM tip exceeds the maximum force that the membrane could withstand, the AFM tip penetrates the membrane (point 'C' to 'D'). After point 'D', the AFM probe starts to interact with the hard mica substrate. The discontinuity between point 'C' and 'D' is a characteristic for an AFM tip[77] penetrating a lipid bilayer membrane[78]. The maximum force that a lipid bilayer membrane withstands before its rupture is the yield threshold force which indicates the lipid bilayer membrane's stability under compression[78–80]. The breakthrough distance (separation between point "C" and "D") relates to membrane thickness[81–87].

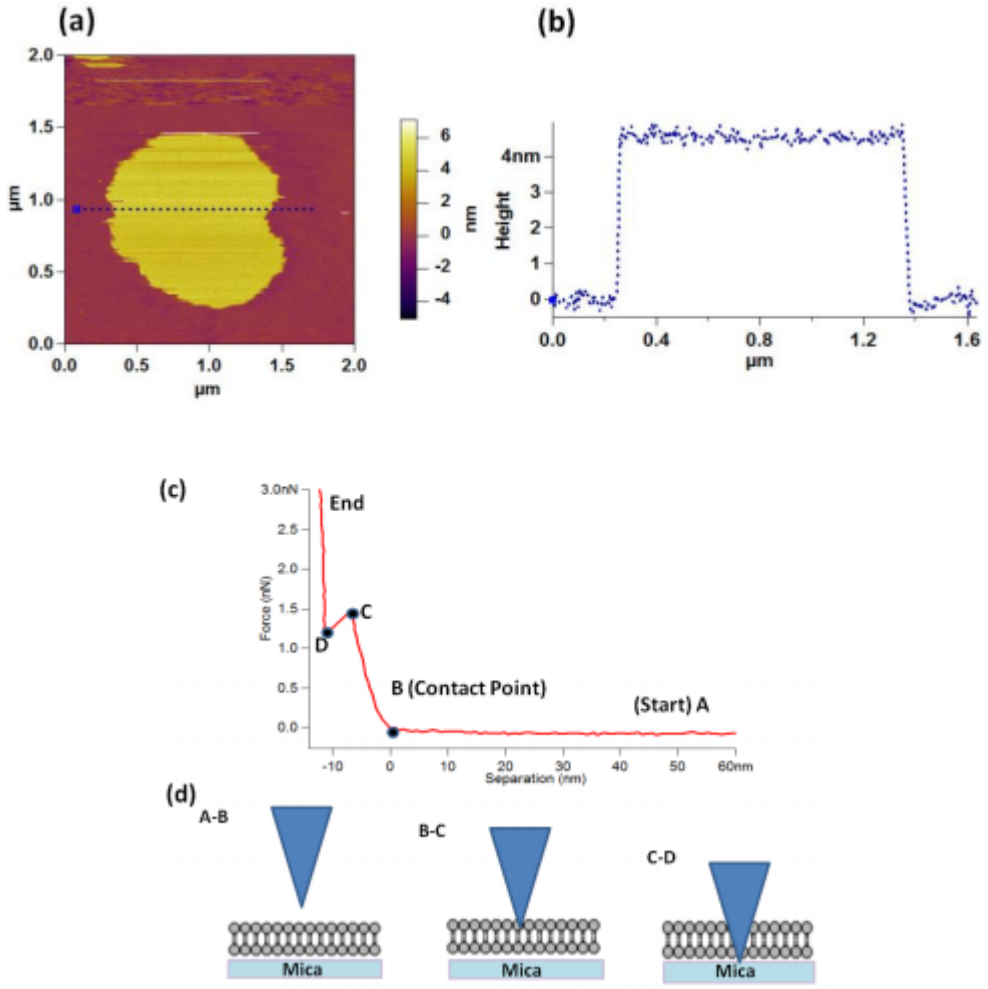

Figure 3. (a) AFM topography images of tethered LBM on TS Au; (b) Line profile corresponding to the blue line shown in (a); (c) A representative force curve (extension portion) obtained on the yellow feature shown in (a); and (d) Schematic of tip-LBM interaction in force measurements.[14]

In summary, a breakthrough point is the point at which the AFM tip punctures the membrane surface. It appears in an AFM-Force spectroscopy curve as the sudden dip, which indicates the sudden increase in force as the AFM tip encounters resistance from the vesicle membrane, until the membrane's resistance threshold is overcome, at which point, as the AFM tip punctures the membrane, the resistance is gone, as represented by the sudden decrease in force in the force curve, which then gradually increases again as the AFM tip approaches the membrane surface or

a new interface. For a single-layer membrane we have only one membrane layer, therefore only one jump in the curve is exhibited as shown in Figure 3c. For a double-layer membrane or vesicle, we have two membrane layers, therefore two distinct jumps in the data is expected (Figure 4fA). In Figure 4fA we have a sample AFM force-distance curve exhibiting two double breakthrough points.

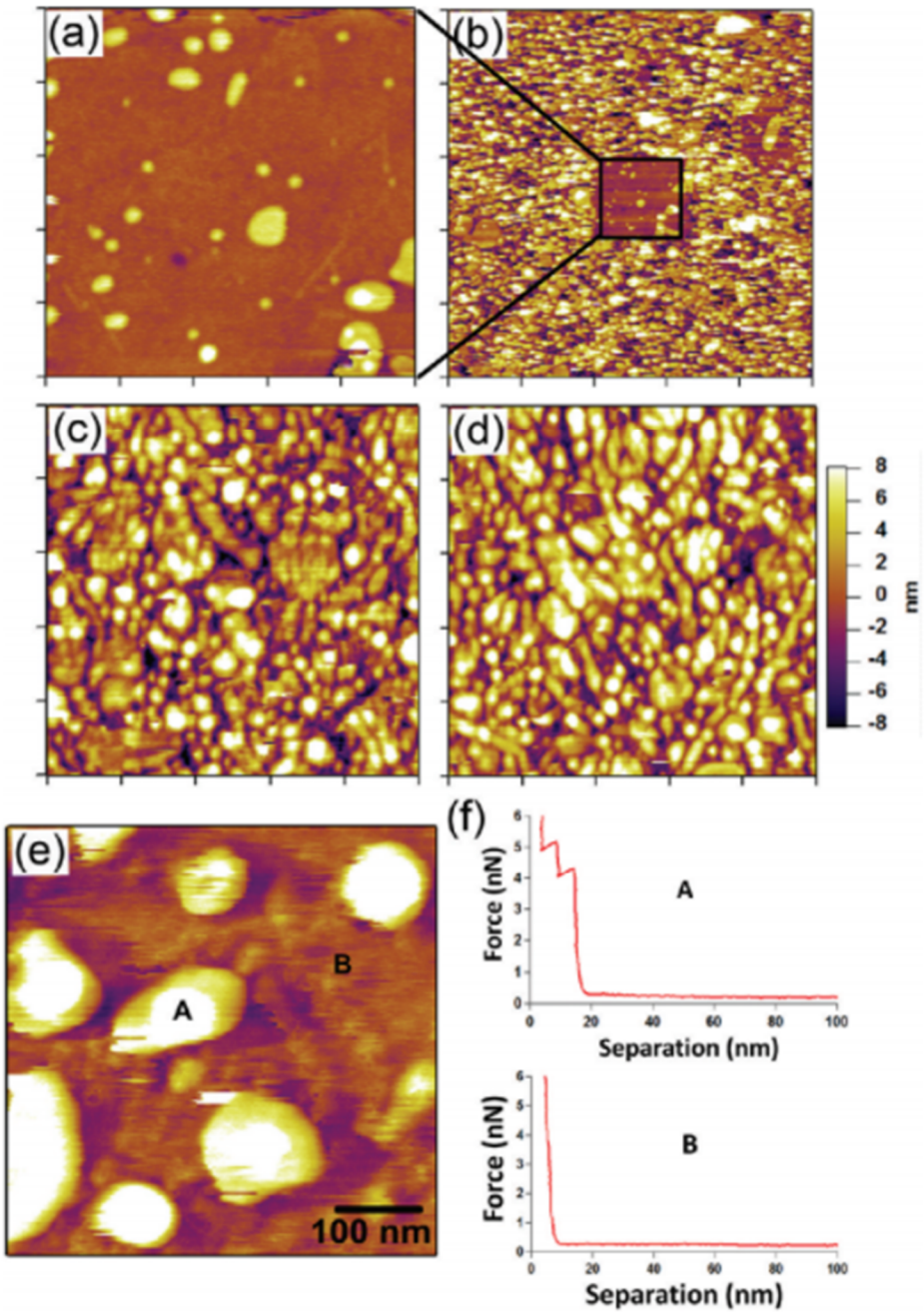

Figure 4. (a) 1 μm × 1 μm AFM topography images of TS Au after exposure to 2.5% DSPE-PEG-PDP/97.5% POPC vesicles for 30 min at room temperature and after 20 min of continuous AFM scanning. (b) 5 μm × 5 μm AFM topography image where the scan region of panel a is highlighted with a black square. (c,d) 1 μm × 1 μm AFM topography images of 100% POPC on oxygen plasma treated TS Au after a 30 min incubation period at room temperature and after 20 min of continuous tapping mode scanning, respectively. (e) Higher resolution AFM topography image of POPC/ TS Au obtained after 20 min of continuous tapping-mode scanning. (f) Force−distance curves corresponding to two areas shown in panel (e).[76]

3.3.2 Algorithm

Force-separation data obtained from AFM force spectroscopy were analyzed using an algorithm developed in Wolfram Mathematica 10.0 with assistance from Dr. Robert N. Sanderson, which processed raw force spectroscopy curves obtained from 1-palmitoyl-2-oleoyl-*sn*-glycero-3-phosphocholine (POPC) vesicles grafted with 1,2-distearoyl-*sn*-glycero-3-phosphoethanolamine-*N*-poly(ethylene glycol)-2000-*N*-[3-(2-pyridyldithio) propionate] (DSPE-PEG-PDP) at various concentrations (i.e., 0 mol%, 2.5 mol%, 5 mol%, 10 mol%). Force mapping in a 32 × 32 array grid pattern was performed at randomly-approached sample positions. Only double breakthrough points were considered, since a double-breakthrough event indicates the AFM tip ruptures two lipid bilayer membranes, which suggests the existence of a vesicle at that point. Our algorithm processes raw force spectroscopy curves and extracts critical points of interest (POI), such as the hard wall and rupture point, with which we evaluated the vesicle size, breakthrough distance, and breakthrough force of the vesicles scanned. The algorithm first identified the hardwall as the vertical line formed by the points approaching the asymptote representing the AFM tip's contact with the sample surface; the average of the points forms a vertical line with a slope of infinity.

It then identified the critical points when the slope changed sign; in other words, when slope changes from a positive to a negative as well as from a negative to a positive, the slope change was marked as a POI. The contact point was determined by locating the point at which the change in slope was greater than a background noise level that normalized to a slope of zero. More details can be found in Appendix A.

A unique aspect of our algorithm is our double verification method: the program locates points of interest, and a user can also review the respective curve, and then correct the identified point of interest in case there are machine identification errors. Figure 5 is an image of a force distance curve with a double breakthrough; the machine has already identified points of interest (POI), and our user dialog allows the user to manually correct the location of the vertical lines in case there are any misidentifications by the computer. To extract the modulus data from the force curves, the slope of the unloading curve was found, located between BRK 4 and Contact Point (Figure 5). More details can be found in Appendix A.

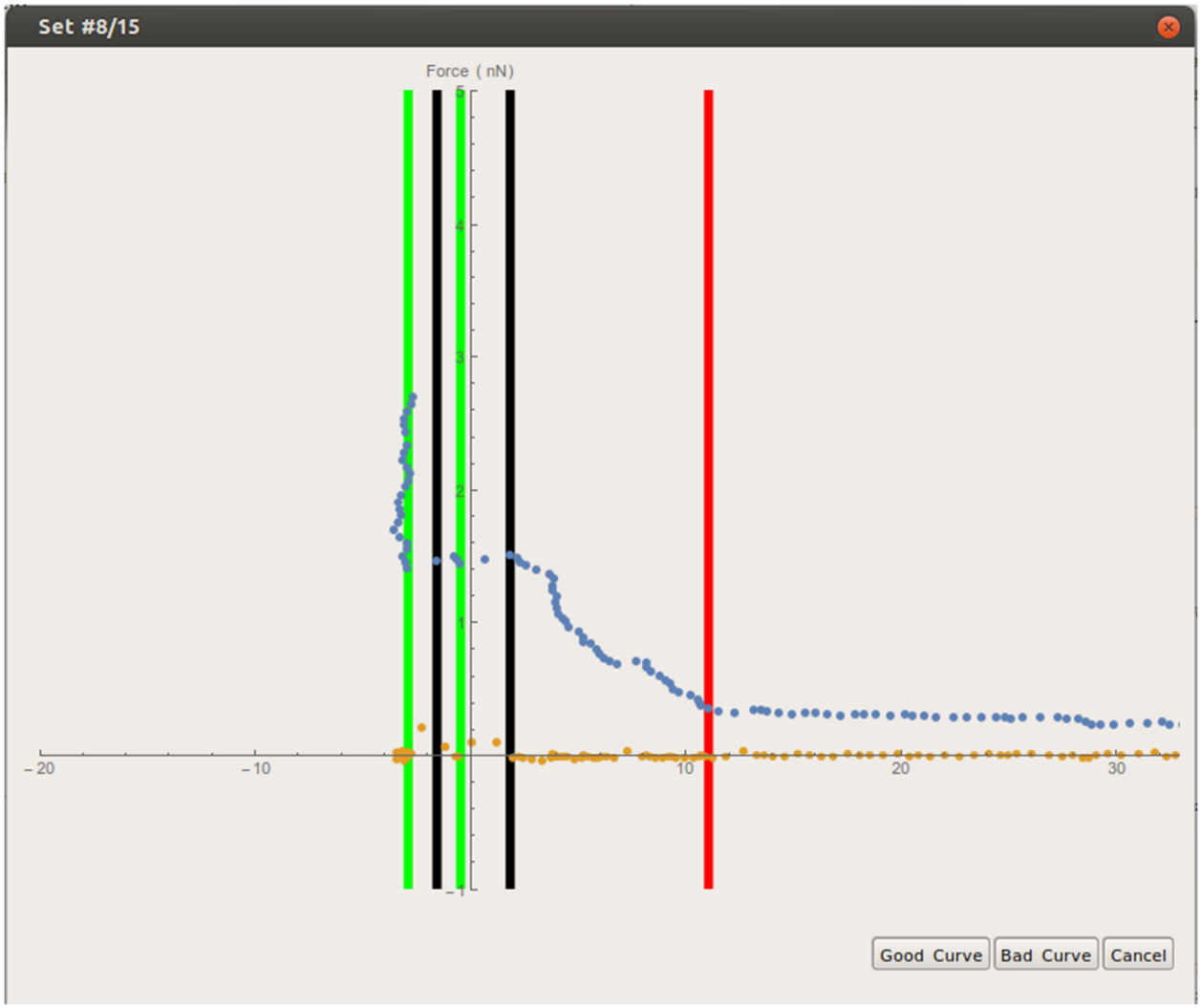

Figure 5. User Dialog indicates and allows user to identify points of interest.

CHAPTER 4. RESULTS & DISCUSSION

When we increase the concentration of DSPE-PEG-PDP relative to POPC, more DSPE-PEG-PDP molecules are embedded in the POPC vesicle membrane, which should affect various vesicle properties, such as size and stiffness. Figure 6 is a schematic of POPC vesicles (blue and yellow) embedded with DSPE-PEG-PDP molecules (red) at various mol% concentrations.

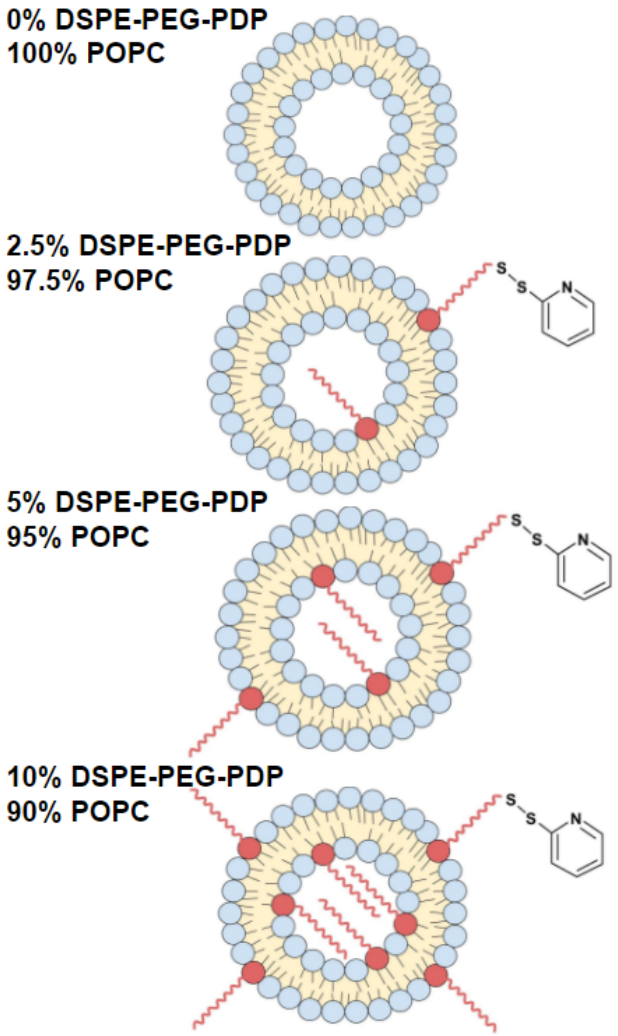

Figure 6. Schematic of POPC vesicles (blue and yellow) embedded with DSPE-PEG-PDP molecules (red) at various mol% concentrations.

4.1 Vesicle Size

We define vesicle size as the distance between the hardwall and the contact point. In Figure 7 we have histograms of the relative frequency of vesicle size (nm) with a bin size of 20 nm for DSPE-PEG-PDP/POPC concentrations varying from 0%, 2.5%, 5%, to 10%. One can see the trend that vesicle size decreases as DSPE-PEG-PDP/POPC concentration increases from 0%, 2.5%, 5%, to 10% (Figure 7). This is attributed to steric hindrance; since DSPE is embedded in the POPC membrane, PEG-PDP molecules occupy space outside of POPC vesicles, and crowding from PEG-PDP molecules causes the relatively more stable smaller POPC molecules to form.

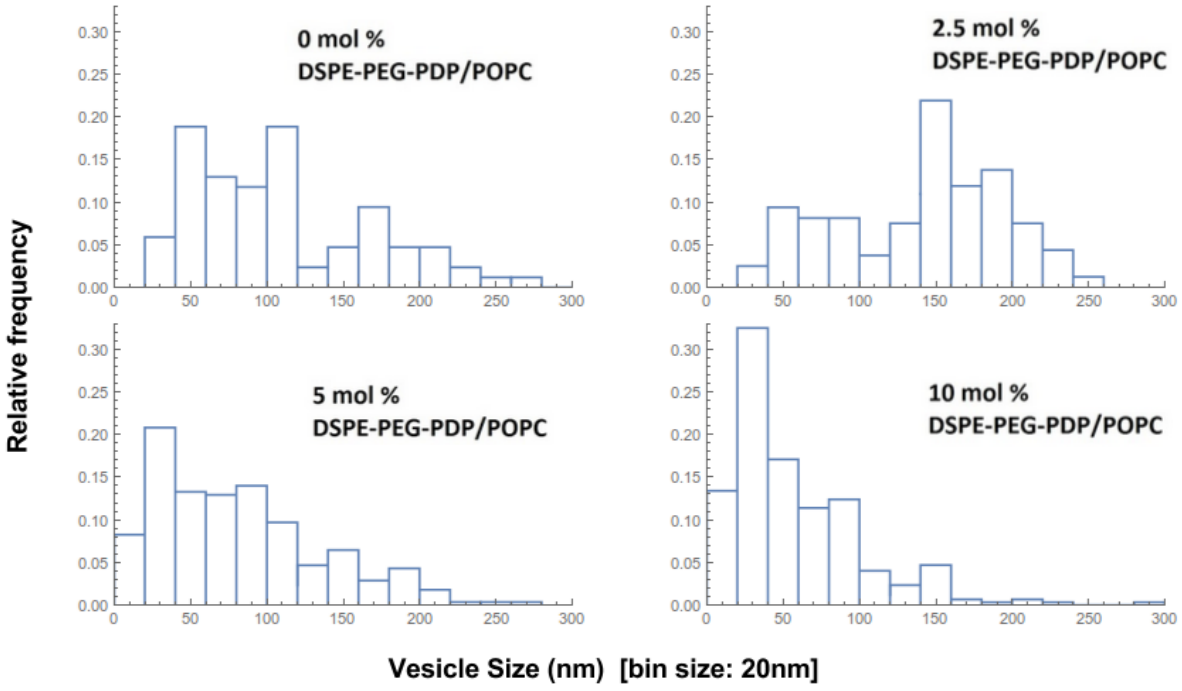

Figure 7. Relative frequency of vesicle size (in nanometers) for DSPE-PEG-PDP/POPC concentrations at (a) 0%, (b) 2.5%, (c) 5%, and (d) 10%.

4.2 Breakthrough Distance

In Figure 8 we have histograms displaying the relative frequency of breakthrough distances (nm) with bin sizes of 2 nm for DSPE-PEG-PDP/POPC concentrations varying from 0%, 2.5%, 5%, to 10%. Breakthrough distance, which is the distance from the hard wall (i.e., average of points aligned parallel to the y-axis in force curves) to breakthrough point, increases with increasing concentration of DSPE-PEG-PDP/POPC (Figure 8). Since DSPE is embedded in the POPC membrane, and PEG-PDP molecules will occupy space outside of POPC vesicles, we propose that this trend is due to steric hindrance from them, which increases breakthrough distance as occupied volume increases with increased DSPE-PEG-PDP concentration.

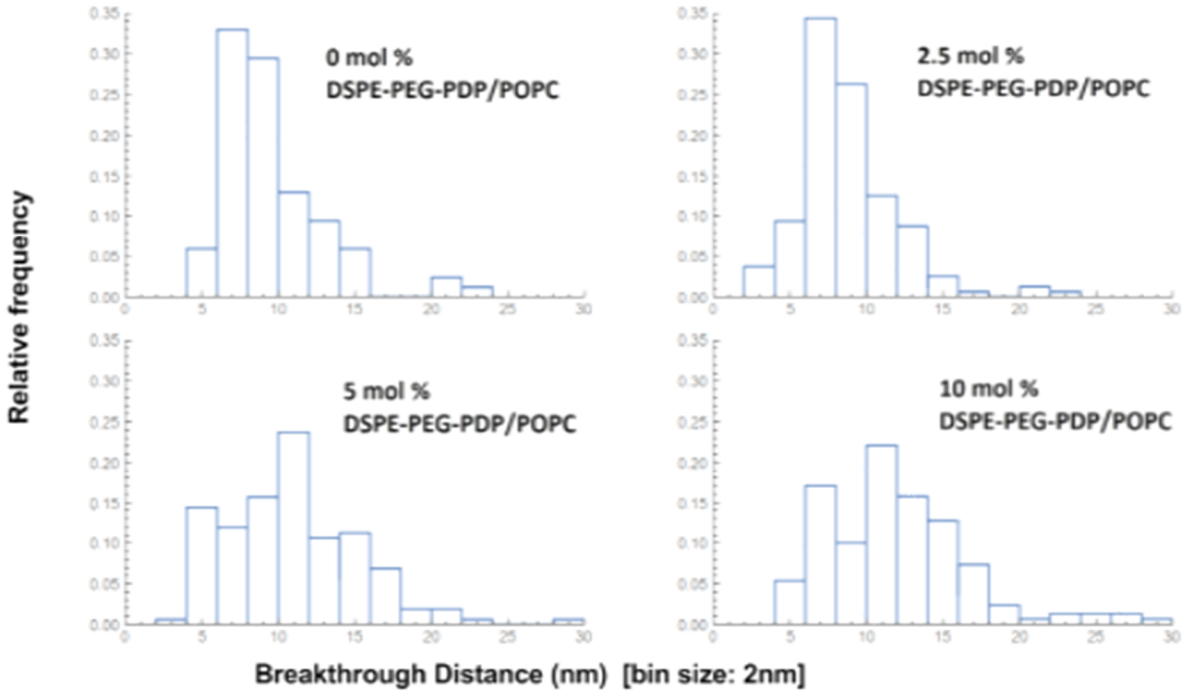

Figure 8. Relative frequency of breakthrough distance (in nanometers) for DSPE-PEG-PDP/POPC concentrations at (a) 0%, (b) 2.5%, (c) 5%, and (d) 10%.

4.3 Breakthrough Force

In Figure 9 we have histograms displaying the relative frequency of breakthrough force (nN) with bin sizes of 0.1 nN for DSPE-PEG-PDP/POPC concentrations varying from 0%, 2.5%, 5%, to 10%. Breakthrough force decreases with increased DSPE-PEG-PDP/POPC concentration (Figure 9). In one study it was proposed that breakthrough force decreased, because of membrane instability introduced by higher temperatures[73,86], therefore the disruptive effect of introducing DSPE-PEG-PDP molecules to a previously-homogeneous POPC membrane layer appears to introduce a similar disorder that creates the membrane instability causing breakthrough force to decrease.

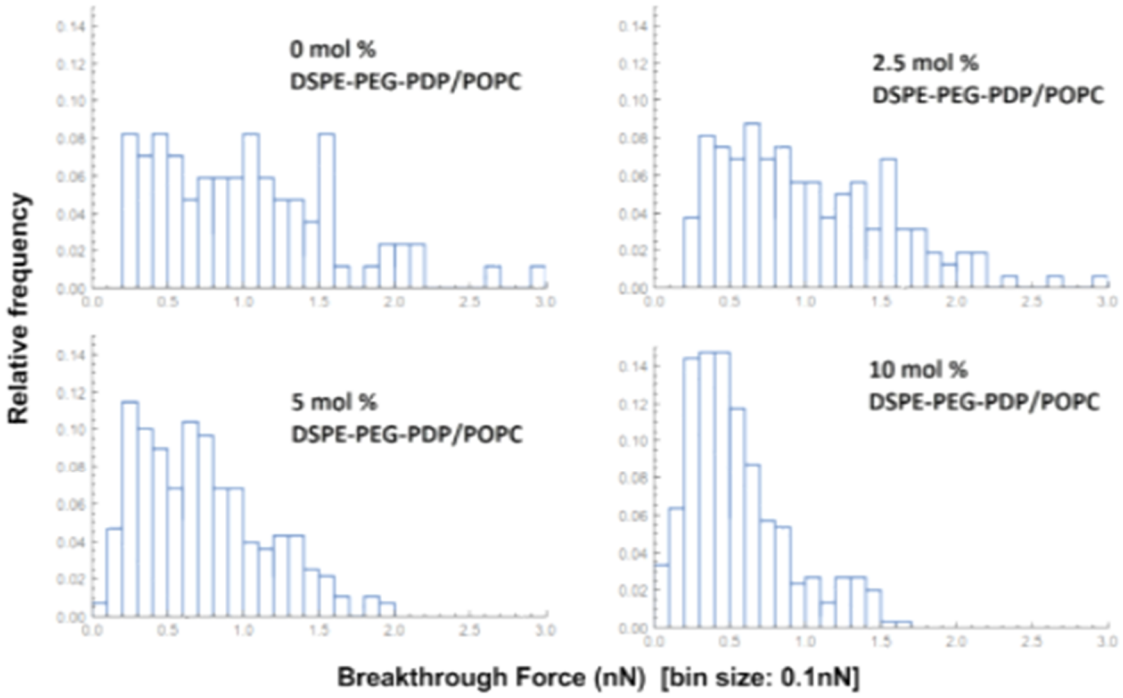

Figure 9. Relative frequency of breakthrough force (in nanoNewtons) for DSPE-PEG-PDP/POPC concentrations at (a) 0%, (b) 2.5%, (c) 5%, and (d) 10%.

4.4 Young's Modulus

The Young's modulus E can be extracted from the slope of the initial linear region of the experimental curves[88] according to the thin shell formula[89]

$$F(\delta) = k_{NV}\delta \quad \text{with} \quad k_{NV} = \frac{\alpha E t^2}{R_{NV}}$$

using the average thickness t from force curves and the radius of curvature R_{NV} of nanovesicles absorbed on the substrate considered as spherical caps[90]

$$R_{NV} = \frac{h_{NV}{}^2 + w_{NV}{}^2/4}{2h_{NV}}$$

with the height h_{NV} values from force curves and taking the topographical width w_{NV} from the topographic profile in the middle of the nanovesicles at the beginning of the experiment[88] and estimates giving $\alpha = 1.73$.[91]

In Figure 10 we compare two plots which plot the slope (nN/nm) versus vesicle diameter (nm) (Figure 10a) as well as the (Slope)×(vesicle diameter) (nN) versus vesicle diameter (nm) (Figure 10b) for a concentration of DSPE-PEG-PDP/POPC at 0%. When we plot measured slope values in the linear region, such as for 0% functionalized vesicles (Figure 10a), we see a curve that appears logarithmic. When the slope is multiplied by the vesicle diameter, which also represents tip indentation, the y-axis is closer to being constant, especially for larger vesicles (>100nm diameter). Flattening the curves by multiplying the slopes with vesicle diameter helps simplify our analysis, especially when we compare different concentrations (Figure 11).

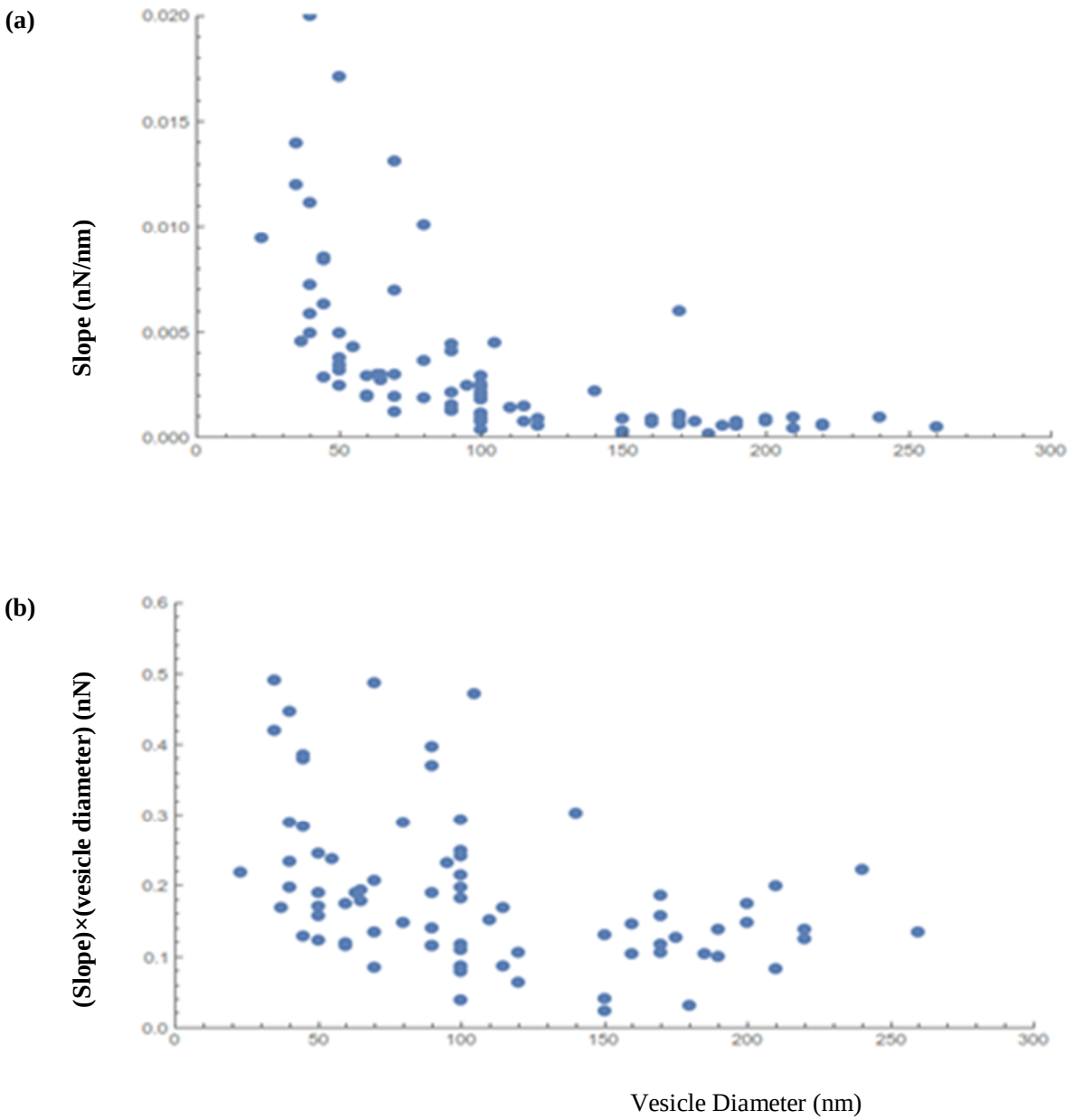

Figure 10. For 0% functionalized vesicles (a) Slope (nN/nm) vs. vesicle diameter (nm); (b) (Slope)x(vesicle diameter) vs. vesicle diameter (nm).

In Figure 11, we compare the (Slope)×(vesicle diameter) (nN) versus vesicle diameter (nm) for a concentrations of DSPE-PEG-PDP/POPC at 0%, 2.5%, 5%, and 10%, because we are interested in seeing the differences between the different concentrations. To simplify our analysis and comparison of different concentrations, we flatten the curves for DSPE-PEG-PDP/POPC concentrations of 0% DSPE-PEG-PDP/100% POPC, 2.5% DSPE-PEG-PDP/97.5% POPC, 5% DSPE-PEG-PDP/95% POPC, and 10% DSPE-PEG-PDP/90% POPC by multiplying the slopes with vesicle diameter (Figure 11). We see a two-peak trend that suggests two distinct conformations are simultaneously present at 5%.

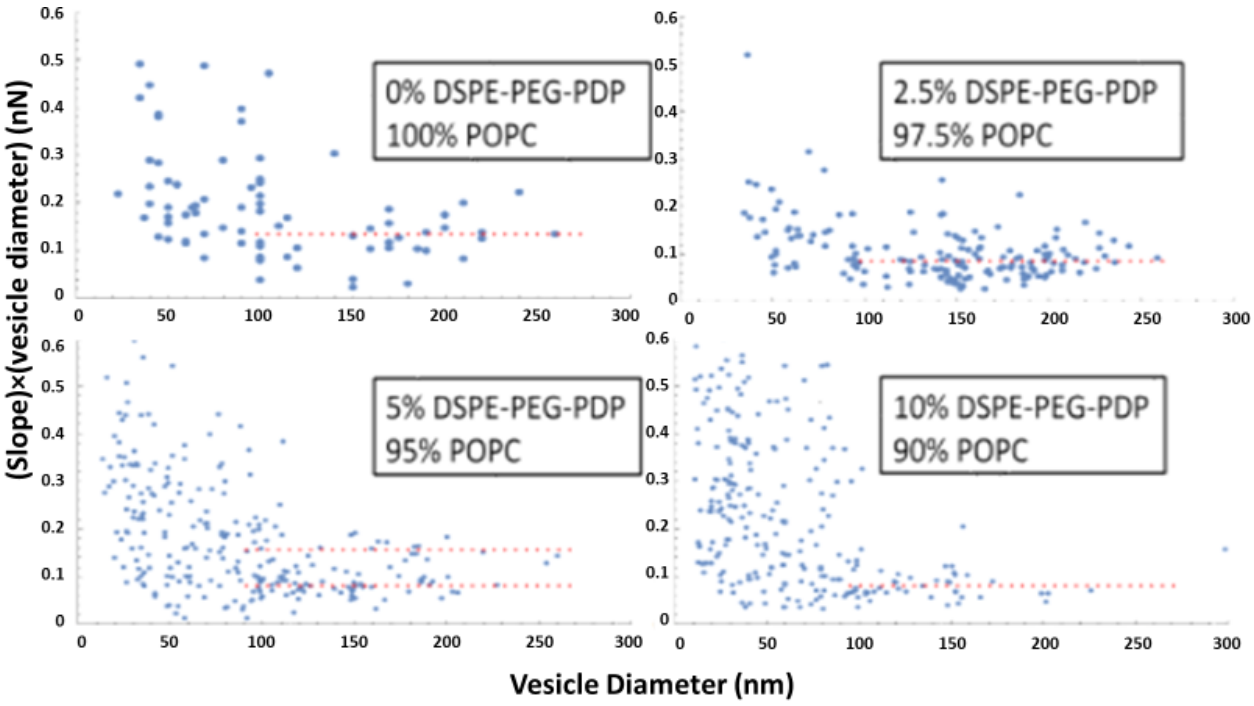

Figure 11. Mathematically flattened regions for DSPE-PEG-PDP/POPC concentrations of (a) 0 mol% DSPE-PEG-PDP/100 mol% POPC, (b) 2.5 mol% DSPE-PEG-PDP/97.5 mol% POPC, (c) 5 mol% DSPE-PEG-PDP/95 mol% POPC, and (d) 10 mol% DSPE-PEG-PDP/90 mol% POPC.

In Figure 12, we consolidate the information from the plots displayed in Figure 11 into one plot. After using the thin shell numerical model and inserting numerical parameters as described by Calò[88], we observed a relative elasticity trend across concentrations of 0%, 2.5%, 5%, and 10% for vesicles over 100 nm in height that includes two distinct values at 5% (Figure 12).

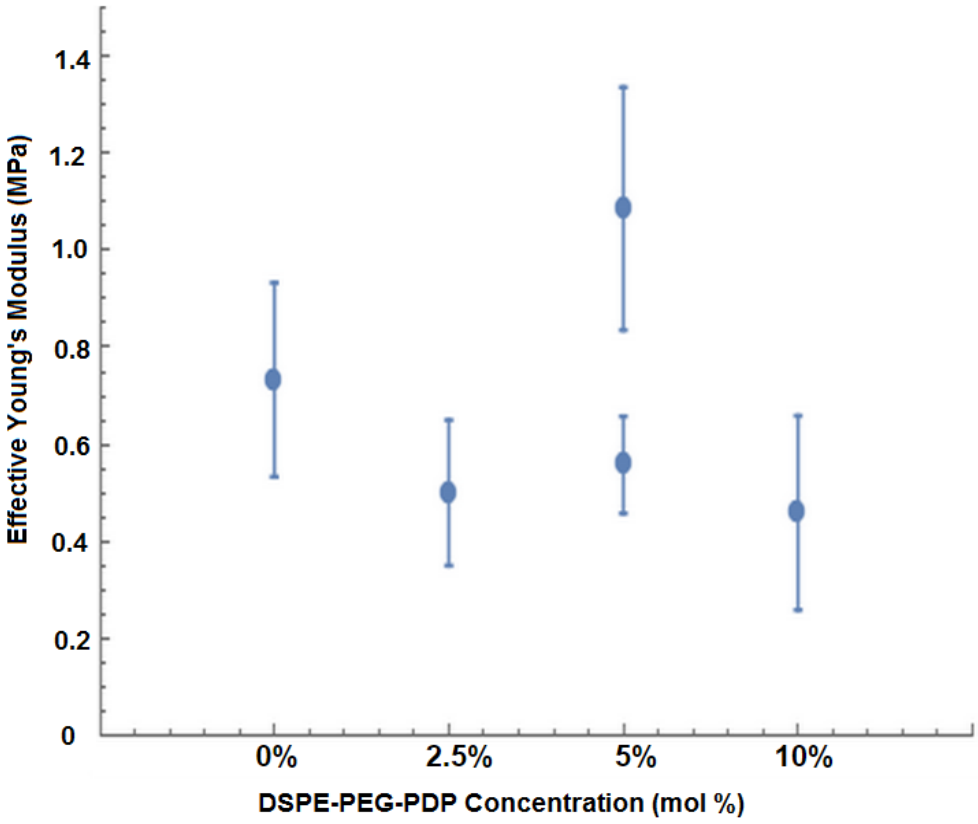

Figure 12. Relative elasticity trend across concentrations of 0%, 2.5%, 5%, and 10% DSPE-PEG-PDP/POPC. 0% has 11 force maps, with 210 to 256 force-distance curves for each force map; 2.5% has 25 force maps with 132 to 240 force-distance curves for each force map; 5% has 5 force maps with 1023 to 1024 force-distance curves for each force map; 10% has 6 force maps with 1023 to 1024 force-distance curves for each force map..

Experiments have shown that PEG chain conformations exhibit a mushroom-to-brush phase transition between 2.5 mol% and 10 mol% concentrations for tethered lipid bilayer membranes assembled on atomically-flat template-stripped gold surfaces[92]. In Figure 13 we see the relationship between the Young's modulus, DSPE-PEG-PDP concentration (mol%), and the schematic illustration of tLBM structures with lipid composition of (a) 100% POPC; (b) 1−6% DSPE-PEG-PDP/99− 95% POPC; (c) 8−10% DSPE-PEG-PDP/92−90% POPC, and (d) 24% DSPE-PEG-PDP/76% POPC [92].

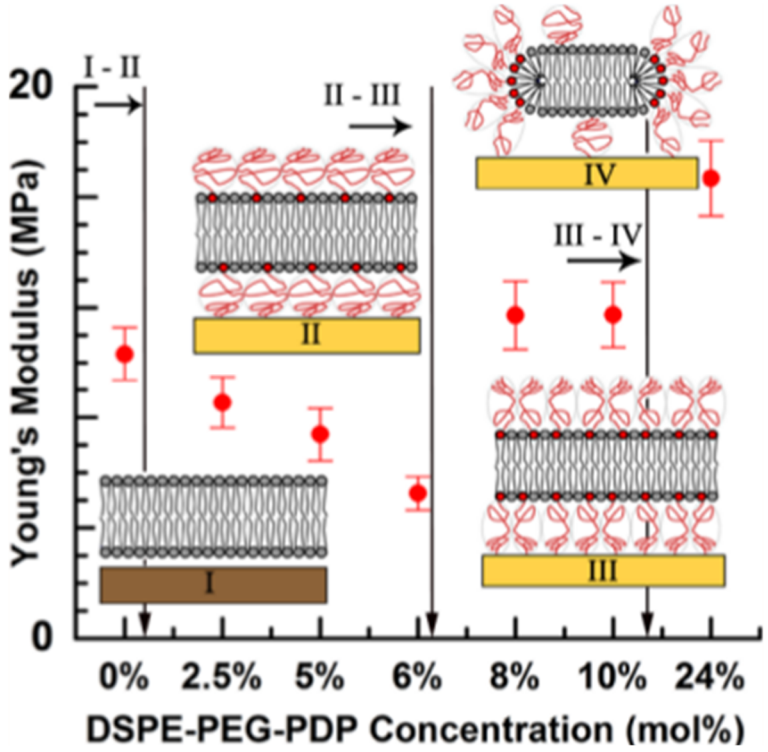

Figure 13. Relationship between Young's modulus, DSPE-PEG-PDP concentration (mol%), and the schematic illustration of tLBM structures with lipid composition of (a) 100% POPC; (b) 1−6% DSPE-PEG-PDP/99− 95% POPC; (c) 8−10% DSPE-PEG-PDP/92−90% POPC, and (d) 24% DSPE-PEG-PDP/76% POPC[92].

There is an abrupt increase in E after the mushroom-to-brush phase transition due to increased PEG grafting density. E was found to be directly correlated with PEG chain conformation.

Results show an initial decrease in tLBM elastic modulus with respect to supported POPC LBM, and then an abrupt increase at a DSPE-PEG-PDP concentration of 8% after the mushroom-to-brush transition has been reported to occur[92–94]. Higher concentrations of DSPE-PEG-PDP, up to 24%, results in a further increase in E, and a structural change, also associated with a phase transition, is observed in AFM topography[92]. AFM topography data indicate that PEG chains segregate at the rim of bilayer disks at 24% DSPE-PEG-PDP concentration[92].

The impact of PEG grafting density on E values, especially with the existence of a mushroom-to-brush conformation phase transition, suggests that the existence of two E values for 5% vesicles is due to the existence of a mushroom-to-brush transition phase as well, and two distinct E values represent the existence of two distinct vesicle conformations at 5 mol% concentration.

CHAPTER 5. CONCLUSION

Investigating the mechanical behavior of lipid bilayer membranes is essential to understanding the dynamics of cell and vesicle behavior. The mechanical properties of 1-palmitoyl-2-oleoyl-*sn*-glycero-3-phosphocholine (POPC) vesicles grafted with different 1,2-distearoyl-*sn*-glycero-3-phosphoethanolamine-*N*-poly(ethylene glycol)-2000-*N*-[3-(2-pyridyldithio) propionate] (DSPE-PEG-PDP) concentrations were studied using AFM force spectroscopy under buffer environment. The concentration of DSPE-PEG-PDP incorporated into POPC vesicles was systematically varied from 0 mol% to 10 mol%. By increasing DSPE-PEG-PDP concentration from 0 – 10 mol%, vesicle size decreases, breakthrough distance increases, breakthrough force decreases, and the Young's modulus (E) decreases slightly. PEG-grafted vesicles are sterically stabilized due to the presence of dangling PEG chains outside the vesicle membrane. We also observe two E values exist at 5 mol%, suggesting the existence of two distinct conformations at 5 mol% concentration. Future experiments investigating the impact of phase transitions, ions, and hydration on vesicle formation can further elucidate the distinct mechanical behavior of DSPE-PEG-PDP/POPC vesicles.

REFERENCES

1. Kasas, S. & Dietler, G. Probing nanomechanical properties from biomolecules to living cells. *Pflüg. Arch. - Eur. J. Physiol.* **456,** 13–27 (2008).
2. Raman, A. *et al.* Mapping nanomechanical properties of live cells using multi-harmonic atomic force microscopy. *Nat. Nanotechnol.* **6,** 809–814 (2011).
3. Nelson, C. M. *et al.* Emergent patterns of growth controlled by multicellular form and mechanics. *Proc. Natl. Acad. Sci.* **102,** 11594–11599 (2005).
4. Nayyar, A., Walker, G., Canetta, E., Wardrop, F. & Adya, A. K. Influence of Cell Surface and Nanomechanical Properties on the Flocculation Ability of Industrial Saccharomyces cerevisiae Strains. *J. Food Res.* **6,** 1 (2017).
5. Dembo, M. & Wang, Y.-L. Stresses at the Cell-to-Substrate Interface during Locomotion of Fibroblasts. *Biophys. J.* **76,** 2307–2316 (1999).
6. du Roure, O. *et al.* Force mapping in epithelial cell migration. *Proc. Natl. Acad. Sci.* **102,** 2390–2395 (2005).
7. Palm, K., Luthman, K., Unge, A.-L., Strandlund, G. & Artursson, P. Correlation of Drug Absorption with Molecular Surface Properties. *J. Pharm. Sci.* **85,** 32–39 (1996).
8. Breukink, E. *et al.* Use of the Cell Wall Precursor Lipid II by a Pore-Forming Peptide Antibiotic. *Science* **286,** 2361–2364 (1999).
9. Fantner, G. E., Barbero, R. J., Gray, D. S. & Belcher, A. M. Kinetics of antimicrobial peptide activity measured on individual bacterial cells using high-speed atomic force microscopy. *Nat. Nanotechnol.* **5,** 280–285 (2010).

10. Rotsch, C. & Radmacher, M. Drug-Induced Changes of Cytoskeletal Structure and Mechanics in Fibroblasts: An Atomic Force Microscopy Study. *Biophys. J.* **78,** 520–535 (2000).
11. Ingber, D. E. Tensegrity: The Architectural Basis of Cellular Mechanotransduction. *Annu. Rev. Physiol.* **59,** 575–599 (1997).
12. Suresh, S. Biomechanics and biophysics of cancer cells. *Acta Mater.* **55,** 3989–4014 (2007).
13. Tan, J. L. *et al.* Cells lying on a bed of microneedles: An approach to isolate mechanical force. *Proc. Natl. Acad. Sci.* **100,** 1484–1489 (2003).
14. Wang, X. Fundamental Studies of Assembly and Mechanical Properties of Lipid Bilayer Membranes and Unilamellar Vesicles. *PhD Thesis* (2013).
15. Brochu, H. & Vermette, P. Young's Moduli of Surface-Bound Liposomes by Atomic Force Microscopy Force Measurements. *Langmuir* **24,** 2009–2014 (2008).
16. Ngwa, W., Chen, K., Sahgal, A., Stepanov, E. V. & Luo, W. Nanoscale mechanics of solid-supported multilayered lipid films by force measurement. *Thin Solid Films* **516,** 5039–5045 (2008).
17. Wagner, M. L. & Tamm, L. K. Tethered Polymer-Supported Planar Lipid Bilayers for Reconstitution of Integral Membrane Proteins: Silane-Polyethyleneglycol-Lipid as a Cushion and Covalent Linker. *Biophys. J.* **79,** 1400–1414 (2000).
18. Munro, J. C. & Frank, C. W. In Situ Formation and Characterization of Poly(ethylene glycol)-Supported Lipid Bilayers on Gold Surfaces. *Langmuir* **20,** 10567–10575 (2004).
19. Munro, J. C. & Frank, C. W. Adsorption of Lipid-Functionalized Poly(ethylene glycol) to Gold Surfaces as a Cushion for Polymer-Supported Lipid Bilayers. *Langmuir* **20,** 3339–3349 (2004).

20. Biebuyck, H. A. & Whitesides, G. M. Interchange between monolayers on gold formed from unsymmetrical disulfides and solutions of thiols: evidence for sulfur-sulfur bond cleavage by gold metal. *Langmuir* **9,** 1766–1770 (1993).
21. Neuman, K. C. & Nagy, A. Single-molecule force spectroscopy: optical tweezers, magnetic tweezers and atomic force microscopy. *Nat. Methods* **5,** 491–505 (2008).
22. Delorme, N. & Fery, A. Direct method to study membrane rigidity of small vesicles based on atomic force microscope force spectroscopy. *Phys. Rev. E* **74,** 030901 (2006).
23. Vogel, V. & Sheetz, M. Local force and geometry sensing regulate cell functions. *Nat. Rev. Mol. Cell Biol.* **7,** 265–275 (2006).
24. Chen, C. S., Tan, J. & Tien, J. Mechanotransduction at Cell-Matrix and Cell-Cell Contacts. *Annu. Rev. Biomed. Eng.* **6,** 275–302 (2004).
25. Praetorius, H. A. & Spring, K. R. A Physiological View of the Primary Cilium. *Annu. Rev. Physiol.* **67,** 515–529 (2005).
26. Tschumperlin, D. J. *et al.* Mechanotransduction through growth-factor shedding into the extracellular space. *Nature* **429,** 83–86 (2004).
27. Ursell, T., Kondev, J., Reeves, D., Wiggins, P. A. & RobPhillips, R. Role of Lipid Bilayer Mechanics in Mechanosensation. in 37–70 (Springer, Dordrecht, 2008). doi:10.1007/978-1-4020-6426-5_2
28. Phillips, R., Ursell, T., Wiggins, P. & Sens, P. Emerging roles for lipids in shaping membrane-protein function. (2009). doi:10.1038/nature08147
29. Lundbæk, J. A., Birn, P., Girshman, J., Hansen, A. J. & Andersen, O. S. Membrane Stiffness and Channel Function. *Biochemistry (Mosc.)* **35,** 3825–3830 (1996).

30. Binnig, G., Quate, C. F. & Gerber, C. Atomic Force Microscope. *Phys. Rev. Lett.* **56,** 930–933 (1986).

31. Parot Pierre *et al.* Past, present and future of atomic force microscopy in life sciences and medicine. *J. Mol. Recognit.* **20,** 418–431 (2007).

32. Dufrêne, Y. F. Towards nanomicrobiology using atomic force microscopy. *Nat. Rev. Microbiol.* **6,** 674–680 (2008).

33. Müller, D. J. & Dufrêne, Y. F. Atomic force microscopy as a multifunctional molecular toolbox in nanobiotechnology. *Nat. Nanotechnol.* **3,** 261–269 (2008).

34. Rico, F., Picas, L., Colom, A., Buzhynskyy, N. & Scheuring, S. The mechanics of membrane proteins is a signature of biological function. *Soft Matter* **9,** 7866–7873 (2013).

35. Lee, G. U., Chrisey, L. A. & Colton, R. J. Direct measurement of the forces between complementary strands of DNA. *Science* **266,** 771–773 (1994).

36. Corcoran, S. G., Colton, R. J., Lilleodden, E. T. & Gerberich, W. W. Anomalous plastic deformation at surfaces: Nanoindentation of gold single crystals. *Phys. Rev. B* **55,** R16057–R16060 (1997).

37. Fisher, T. E., Oberhauser, A. F., Carrion-Vazquez, M., Marszalek, P. E. & Fernandez, J. M. The study of protein mechanics with the atomic force microscope. *Trends Biochem. Sci.* **24,** 379–384 (1999).

38. Giannotti Marina I. & Vancso G. Julius. Interrogation of Single Synthetic Polymer Chains and Polysaccharides by AFM-Based Force Spectroscopy. *ChemPhysChem* **8,** 2290–2307 (2007).

39. Janovjak Harald, Sapra K. Tanuj, Kedrov Alexej & Müller Daniel J. From Valleys to Ridges: Exploring the Dynamic Energy Landscape of Single Membrane Proteins. *ChemPhysChem* **9,** 954–966 (2008).

40. Picas, L., Rico, F., Deforet, M. & Scheuring, S. Structural and Mechanical Heterogeneity of the Erythrocyte Membrane Reveals Hallmarks of Membrane Stability. *ACS Nano* **7,** 1054–1063 (2013).

41. Rammensee, S., Kang, M. S., Georgiou, K., Kumar, S. & Schaffer, D. V. Dynamics of mechanosensitive neural stem cell differentiation. *Stem Cells* **35,** 497–506 (2017).

42. Mikulska, K., Strzelecki, J. & Nowak, W. Nanomechanics of β-rich proteins related to neuronal disorders studied by AFM, all-atom and coarse-grained MD methods. *J. Mol. Model.* **20,** 2144 (2014).

43. Krause, M., Riet, J. te & Wolf, K. Probing the compressibility of tumor cell nuclei by combined atomic force–confocal microscopy. *Phys. Biol.* **10,** 065002 (2013).

44. Rother, J., Nöding, H., Mey, I. & Janshoff, A. Atomic force microscopy-based microrheology reveals significant differences in the viscoelastic response between malign and benign cell lines. *Open Biol.* **4,** 140046 (2014).

45. Romero-Vargas Castrillón, S., Perreault, F., de Faria, A. F. & Elimelech, M. Interaction of Graphene Oxide with Bacterial Cell Membranes: Insights from Force Spectroscopy. *Environ. Sci. Technol. Lett.* **2,** 112–117 (2015).

46. Meng, F. & Zhong, Z. Polymersomes Spanning from Nano- to Microscales: Advanced Vehicles for Controlled Drug Delivery and Robust Vesicles for Virus and Cell Mimicking. *J. Phys. Chem. Lett.* **2,** 1533–1539 (2011).

47. Weisenhorn, A. L., Khorsandi, M., Kasas, S., Gotzos, V. & Butt, H.-J. Deformation and height anomaly of soft surfaces studied with an AFM. *Nanotechnology* **4,** 106 (1993).
48. HERTZ, H. On the contact of elastic solids. *Z Reine Angew Math.* **92,** 156–171 (1881).
49. Mahaffy, R. E., Shih, C. K., MacKintosh, F. C. & Käs, J. Scanning Probe-Based Frequency-Dependent Microrheology of Polymer Gels and Biological Cells. *Phys. Rev. Lett.* **85,** 880–883 (2000).
50. Coceano, G. *et al.* Investigation into local cell mechanics by atomic force microscopy mapping and optical tweezer vertical indentation. *Nanotechnology* **27,** 065102 (2016).
51. Zeng, G. *et al.* Functional bacterial amyloid increases Pseudomonas biofilm hydrophobicity and stiffness. *Front. Microbiol.* **6,** (2015).
52. Gregurec, D., Velasco-Lozano, S., E. Moya, S., Vázquez, L. & López-Gallego, F. Force spectroscopy predicts thermal stability of immobilized proteins by measuring microbead mechanics. *Soft Matter* **12,** 8718–8725 (2016).
53. Correia Faria, E. *et al.* Measurement of elastic properties of prostate cancer cells using AFM. *Analyst* **133,** 1498–1500 (2008).
54. Haga, H. *et al.* Elasticity mapping of living fibroblasts by AFM and immunofluorescence observation of the cytoskeleton. *Ultramicroscopy* **82,** 253–258 (2000).
55. C. Nalam, P., N. Gosvami, N., A. Caporizzo, M., J. Composto, R. & W. Carpick, R. Nano-rheology of hydrogels using direct drive force modulation atomic force microscopy. *Soft Matter* **11,** 8165–8178 (2015).
56. Landau, L. D., Pitaevskii, L. P., Kosevich, A. M. & Lifshitz, E. M. *Theory of Elasticity, Third Edition: Volume 7*. (Butterworth-Heinemann, 1986).

57. Dimitriadis, E. K., Horkay, F., Maresca, J., Kachar, B. & Chadwick, R. S. Determination of Elastic Moduli of Thin Layers of Soft Material Using the Atomic Force Microscope. *Biophys. J.* **82,** 2798–2810 (2002).
58. Künneke, S., Krüger, D. & Janshoff, A. Scrutiny of the Failure of Lipid Membranes as a Function of Headgroups, Chain Length, and Lamellarity Measured by Scanning Force Microscopy. *Biophys. J.* **86,** 1545–1553 (2004).
59. Szymonski, M., Targosz-Korecka, M. & Malek-Zietek, K. E. Nano-mechanical model of endothelial dysfunction for AFM-based diagnostics at the cellular level. *Pharmacol. Rep.* **67,** 728–735 (2015).
60. Obiols-Rabasa, M. *et al.* Investigation of the elastic and adhesion properties of adsorbed hydrophobically modified inulin films on latex particles using Atomic Force Microscopy (AFM). *Colloids Surf. Physicochem. Eng. Asp.* **524,** 185–192 (2017).
61. Yun, X. *et al.* Interrogation of drug effects on HeLa cells by exploiting new AFM mechanical biomarkers. *RSC Adv.* **7,** 43764–43771 (2017).
62. Sneddon, I. N. The relation between load and penetration in the axisymmetric boussinesq problem for a punch of arbitrary profile. *Int. J. Eng. Sci.* **3,** 47–57 (1965).
63. Gavara, N. & Chadwick, R. S. Relationship between cell stiffness and stress fiber amount, assessed by simultaneous atomic force microscopy and live-cell fluorescence imaging. *Biomech. Model. Mechanobiol.* **15,** 511–523 (2016).
64. Gavara, N. & Chadwick, R. S. Determination of the elastic moduli of thin samples and adherent cells using conical atomic force microscope tips. *Nat. Nanotechnol.* **7,** 733–736 (2012).

65. Hope, M. J., Bally, M. B., Webb, G. & Cullis, P. R. Production of large unilamellar vesicles by a rapid extrusion procedure. Characterization of size distribution, trapped volume and ability to maintain a membrane potential. *Biochim. Biophys. Acta BBA - Biomembr.* **812,** 55–65 (1985).

66. Lee, S. *et al.* Scanning Tunneling Microscopy of Template-Stripped Au Surfaces and Highly Ordered Self-Assembled Monolayers. *Langmuir* **24,** 5984–5987 (2008).

67. Dufrêne, Y. F., Boland, T., Schneider, J. W., Barger, W. R. & Lee, G. U. Characterization of the physical properties of model biomembranes at the nanometer scale with the atomic force microscope. *Faraday Discuss.* **111,** 79–94 (1999).

68. Alessandrini, A. & Facci, P. AFM: a versatile tool in biophysics. *Meas. Sci. Technol.* **16,** R65 (2005).

69. Alessandrini Andrea & Facci Paolo. Unraveling lipid/protein interaction in model lipid bilayers by Atomic Force Microscopy. *J. Mol. Recognit.* **24,** 387–396 (2011).

70. Alessandrini, A., Seeger, H. M., Caramaschi, T. & Facci, P. Dynamic Force Spectroscopy on Supported Lipid Bilayers: Effect of Temperature and Sample Preparation. *Biophys. J.* **103,** 38–47 (2012).

71. Alessandrini, A. & Facci, P. Nanoscale mechanical properties of lipid bilayers and their relevance in biomembrane organization and function. *Micron* **43,** 1212–1223 (2012).

72. Butt, H.-J. & Franz, V. Rupture of molecular thin films observed in atomic force microscopy. I. Theory. *Phys. Rev. E* **66,** 031601 (2002).

73. Garcia-Manyes, S. & Sanz, F. Nanomechanics of lipid bilayers by force spectroscopy with AFM: A perspective. *Biochim. Biophys. Acta BBA - Biomembr.* **1798,** 741–749 (2010).

74. Li, S., Eghiaian, F., Sieben, C., Herrmann, A. & Schaap, I. A. T. Bending and Puncturing the Influenza Lipid Envelope. *Biophys. J.* **100,** 637–645 (2011).

75. Hutter, J. L. & Bechhoefer, J. Calibration of atomic-force microscope tips. *Rev. Sci. Instrum.* **64,** 1868–1873 (1993).

76. Wang, X., Shindel, M. M., Wang, S.-W. & Ragan, R. Elucidating Driving Forces for Liposome Rupture: External Perturbations and Chemical Affinity. *Langmuir* **28,** 7417–7427 (2012).

77. Ragan, R., Ohlberg, D., Blackstock, J. J., Kim, S. & Williams, R. S. Atomic Surface Structure of UHV-Prepared Template-Stripped Platinum and Single-Crystal Platinum(111). *J. Phys. Chem. B* **108,** 20187–20192 (2004).

78. Dufrêne, Y. F., Barger, W. R., Green, J.-B. D. & Lee, G. U. Nanometer-Scale Surface Properties of Mixed Phospholipid Monolayers and Bilayers. *Langmuir* **13,** 4779–4784 (1997).

79. Richter, R. P., Bérat, R. & Brisson, A. R. Formation of Solid-Supported Lipid Bilayers: An Integrated View. *Langmuir* **22,** 3497–3505 (2006).

80. Canale C., Jacono M., Diaspro A. & Dante S. Force spectroscopy as a tool to investigate the properties of supported lipid membranes. *Microsc. Res. Tech.* **73,** 965–972 (2010).

81. Dufrêne, Y. F. & Lee, G. U. Advances in the characterization of supported lipid films with the atomic force microscope. *Biochim. Biophys. Acta BBA - Biomembr.* **1509,** 14–41 (2000).

82. Franz, V., Loi, S., Müller, H., Bamberg, E. & Butt, H.-J. Tip penetration through lipid bilayers in atomic force microscopy. *Colloids Surf. B Biointerfaces* **23,** 191–200 (2002).

83. Schneider, J. *et al.* Force and Adhesion Measurements between Hydrogen-Bonded Layers of Glycine-Functionalized Amphiphiles. *J. Am. Chem. Soc.* **120,** 3508–3509 (1998).

84. Schneider, J., Barger, W. & Lee, G. U. Nanometer Scale Surface Properties of Supported Lipid Bilayers Measured with Hydrophobic and Hydrophilic Atomic Force Microscope Probes. *Langmuir* **19,** 1899–1907 (2003).

85. Schneider, J., Dufrêne, Y. F., Barger, W. R. & Lee, G. U. Atomic Force Microscope Image Contrast Mechanisms on Supported Lipid Bilayers. *Biophys. J.* **79,** 1107–1118 (2000).

86. Garcia-Manyes, S., Oncins, G. & Sanz, F. Effect of Ion-Binding and Chemical Phospholipid Structure on the Nanomechanics of Lipid Bilayers Studied by Force Spectroscopy. *Biophys. J.* **89,** 1812–1826 (2005).

87. Oncins, G., Garcia-Manyes, S. & Sanz, F. Study of Frictional Properties of a Phospholipid Bilayer in a Liquid Environment with Lateral Force Microscopy as a Function of NaCl Concentration. *Langmuir* **21,** 7373–7379 (2005).

88. Calò, A. *et al.* Force measurements on natural membrane nanovesicles reveal a composition-independent, high Young's modulus. *Nanoscale* **6,** 2275–2285 (2014).

89. Hernando-Pérez Mercedes *et al.* Direct Measurement of Phage phi29 Stiffness Provides Evidence of Internal Pressure. *Small* **8,** 2366–2370 (2012).

90. Chen, Q., Schönherr, H. & Vancso, G. J. Mechanical properties of block copolymer vesicle membranes by atomic force microscopy. *Soft Matter* **5,** 4944–4950 (2009).

91. Michel, J. P. *et al.* Nanoindentation studies of full and empty viral capsids and the effects of capsid protein mutations on elasticity and strength. *Proc. Natl. Acad. Sci.* **103,** 6184–6189 (2006).

92. Wang, X., Sanderson, R. N. & Ragan, R. Evaluation of Young's Modulus of Tethered 1-Palmitoyl-2-oleoyl-sn-glycero-3-phosphocholine Membranes Using Atomic Force Spectroscopy. *J. Phys. Chem. C* **118,** 29301–29309 (2014).

93. Kaufmann, S., Borisov, O., Textor, M. & Reimhult, E. Mechanical properties of mushroom and brush poly(ethylene glycol)-phospholipid membranes. *Soft Matter* **7,** 9267–9275 (2011).
94. Garbuzenko, O., Barenholz, Y. & Priev, A. Effect of grafted PEG on liposome size and on compressibility and packing of lipid bilayer. *Chem. Phys. Lipids* **135,** 117–129 (2005).

APPENDIX A: PROGRAM CODE

Data processing was originally done manually, and force curves were noted if they had two breakthrough points.

A user dialog was designed so that the user could simply click through each force curve, and then directly mark on the force curve the five points of interest: (BRK1, BRK2, start of Young's modulus curve, end of Young's modulus curve, contact point)

- PointOfInterest1 = breakthrough point 1
- PointOfInterest2 = breakthrough point 2
- PointOfInterest3 = start of Young's modulus curve
- PointOfInterest4 = end of Young's modulus curve
- PointOfInterest5 = contact point

- The points of interest (POI) are then saved, from which functions extract the POI required for calculation.

Organized functions

- User Filtering: UserFilter3[FilePath_]
  - By displaying the raw data with points of interest superimposed, the function *UserFilter3* prompts the user to approve good data, mark points of interest on the raw data displayed, and then save the data into GoodIndexList.
- Fast Plotting Function: PlotThings[ParsedData_,POI_,Options]
  - The function *PlotThings* outputs listplots of data with points of interest superimposed. Inputs:
    - Parsed Data

- Points of Interest (including contact point)
- (end—OPTIONAL) additional options available, such as:
    - superimposing another plot
        - Default: otherPlot->{}, showOtherPlot ->False
        - Activate: otherPlot->{}, showOtherPlot->True
    - displaying error messages
        - Default: BadHW->False, BadCP->False, BadBRK->False
        - To activate: change 'False' to 'True'
        - Note
            - BadHW = Bad Hard Wall
            - BadCP = Bad Contact Point
            - BadBRK = Bad Breakthrough Point
    - adjusting the plot range
        - Default: customRange->{{-20,100},{-1,5}}
        - To adjust:
            - To change x-axis values, edit {-20(x_min),100(x_max)}
            - To change y-axis values, edit {-1(y_min),5(y_max)}

- Data Importing: ParseFile4[FilePath_]
    - The function *ParseFile4* imports and parses the data located at *FilePath.* The data at *FilePath* must have a header with column names of the form

LineXXXXPointXXXXForce_Ext, LineXXXXPointXXXXSep_Ext. Parsing the data is necessary, because the data's original format is not amenable to data analysis.

- Points Of Interest: PointsOfInterest3[ParsedData_]
  - The function *PointsOfInterest* computes breakthrough locations 1-4 (i.e., corresponding to 2 breakthough events). Identifies points of interest (BRK1-BRK4). Utilizes Compile, and is –6000 times faster than the previous method.
- Contact Point: ContactPoint3[ParsedData_,POI_,Options]
  - Takes ParsedData and PointsOfInterest as inputs, and then computes the contact point, which is appended onto the end of POI.
- Youngs Modulus Calculation: CalculateYoungsModulus2[POI_]
  - Computes Young's modulus by fitting to the Sneddon and BECC models. Note that the only input is POI, which MUST be from ContactPoint3[], with showData->True.
  - Smaller definitions used in calculating Young's Modulus include:
    - *Theta*
    - SneddonForce[*delta*_, EE_]
    - BECCForce[*delta*_, EE_, hh_]
    - FitForm[ParsedData_, coords_]
- Points of Interest – Single Breakthrough: POISB[ParsedData]

- The function *POISB* computes the first two breakthrough points (i.e., the breakthrough point and the hardwall contact point). It takes a parsed data set as an input.

- Data Exporting: ExportData[filePath_]
  - The function *ExportData* exports all objects of the form "bin***", where "***" is an integer, counting from). The file is exported to filePath. The clear function clears out the bins.
- getM[dataList,arb.param.]
  - The function *getM* uses *list_* and *param_* as inputs to determine the slope.
- getPointX(Y)[dataList,xval]
  - The function *GetPointX* re-orders the inputted *dataList* and *xVal.*
  - The function *GetPointY* re-orders the inputted *dataList* and *yVal.*
- phaseChangePoint[dataList]
  - From the inputted dataList (*list_*), the function *phaseChangePoint* takes the slopes (i.e., *dxdx* or *getM*) and the positions of the peaks (*maxs)* to calculate the *phaseChangePoint.*
- Histogram importing and work: SetDirectory[""] => dat0, dat2p5, dat5, dat10, dat24
  - After inputting the directory containing "GoodData" (i.e., data that had been filtered and processed to contain only force curves with satisfactory double breakthrough events), the function *SetDirectory* imports and saves the data into lists with the naming format *d<name of original data file>*.

- "Hard setting" of d* to compile the list of {BRK1, BRK2, start of Young's modulus curve, end of Young's modulus curve} for each respective concentration: d0,d2p5,d5,d10
- Full* Object Loading ("*" is the set number)
    - "full*" objects contain a lot of information. They are of the form:
        - Full* = { { {xyData}, {POI}, {linearFitIndex1, linearFitIndex2, vesicleThickness} }
- Slope (slopeCalc[full_]) and slope time R_{nv} (mRCalc[full_])
    - The function *mRCalc[full_]* uses the input *full_* to generate the value of the slope multiplied by R_{nv}.